Geophysical Journal International

Geophys. J. Int. (2023) **233,** 2067–2083
Advance Access publication 2023 January 27
GJI Seismology

https://doi.org/10.1093/gji/ggad031

Rayleigh wave spectral distortions induced by an anticline structure

Christine El Khoury [1], Hervé Chauris,[1] Alexandre Kazantsev[2] and Vadim Monteiller[3]

[1] *Mines Paris – PSL Research University, Centre de Géosciences,* 77300 *Fontainebleau, France. E-mail: christine_kh@hotmail.com*
[2] *Storengy SAS – EISE/DGSM, Engie Group,* 92270 *Bois-Colombes, France*
[3] *Laboratory of Mechanics and Acoustics (LMA), UMR* 7031 *AMU, CNRS, Centrale Marseille,* 13453 *Marseille Cedex* 13*, France*

Accepted 2023 January 17. Received 2022 November 27; in original form 2022 August 1

SUMMARY

Spectral anomalies in the seismic ambient noise are commonly observed above hydrocarbon reservoirs at frequencies of several Hertz. If properly understood, these anomalies could be a potential indicator for hydrocarbon reservoir exploration or monitoring. Under the assumption that ambient noise mainly consists of surface waves, previous studies showed that the geological structure, rather than the hydrocarbon content, could be the major cause of the observed anomalies for purely elastic waves. This work further explores how Rayleigh waves interact with an anticline structure, a typical geological trap for a hydrocarbon reservoir. We propose an approximate semi-analytical surface wave approach for modelling the spectral anomalies. It is based on the contribution of 1-D local solutions from two different models. The results are compared with those obtained via 3-D numerical simulations using the spectral-element approach in the case of a wavefield dominated by Rayleigh waves. Analysis of the anomalies generated by an anticline structure is performed for different source configurations. It shows that the semi-analytical method provides reasonable spectrum predictions for smooth layered models and under some restrictions on the source distribution. Such a tool allows us to run a larger number of simulations to explore the parameter space and finally provide a general law linking the anticline geometrical parameters and the elastic properties of the medium to the anticline-induced spectral anomaly for the case of fundamental mode Rayleigh waves.

Key words: Numerical modelling; Site effects; Surface waves and free oscillations; Wave propagation.

1 INTRODUCTION

The origin of the seismic ambient noise is classified into two main categories: natural and human sources (Withers *et al.* 1996; Mcnamara & Buland 2004; Lehujeur *et al.* 2015). The low frequency natural noise ($f < 1$ Hz), is generated by ocean activities and large-scale meteorological conditions. Two energy peaks appear in the noise wavefield at approximately 0.07 and 0.14 Hz, corresponding to the primary and secondary microseisms. We refer to Nishida (2017) for a detailed review on this topic. At higher frequencies ($f > 1$ Hz), human activities have a significant contribution. The authors distinguish between 'microseisms' and 'microtremors', corresponding to natural and human sources, respectively. The seismic ambient noise wavefield consists of different types of waves, that is body waves and surface waves (Rayleigh and Love waves). Many authors have studied the composition of ambient noise wavefield on different sites in the world. Bonnefoy-Claudet *et al.* (2006) compared the work of five authors and concluded that the noise is a mix of *P* waves and fundamental and higher modes of Rayleigh waves. While the fundamental mode usually dominates below 1 Hz, the wavefield at higher frequencies is often more complicated. No agreement between authors appears, and no definite conclusion is given. According to Bonnefoy-Claudet *et al.* (2006), the noise composition depends on multiple factors: the location of the source (far or near source), its origin (natural or human), but also the site conditions and soil properties.

Dangel *et al.* (2003) observed ambient noise spectral anomalies characterized by spectral amplification peaks on the vertical component within a specific frequency band (1.5 to 4 Hz) above 15 hydrocarbon reservoirs at different locations in the world. An industrial application has been developed with the so-called 'Low Frequency Passive Seismic' method which analyses the spectrum of the ambient seismic noise recorded with broad-band seismometers. Useful information for locating potential hydrocarbon reservoirs is extracted from ambient noise spectral signatures that may be indicators of hydrocarbon presence. Various spectral attributes characterizing the anomalies were proposed. The observations motivated many researchers to study the physical origin of the observed anomalies (Hanssen & Bussat 2008; Holzner *et al.* 2009; Lambert *et al.* 2009; Saenger *et al.* 2009; Riahi *et al.* 2013). However, the studies showed different controversial explanations implying

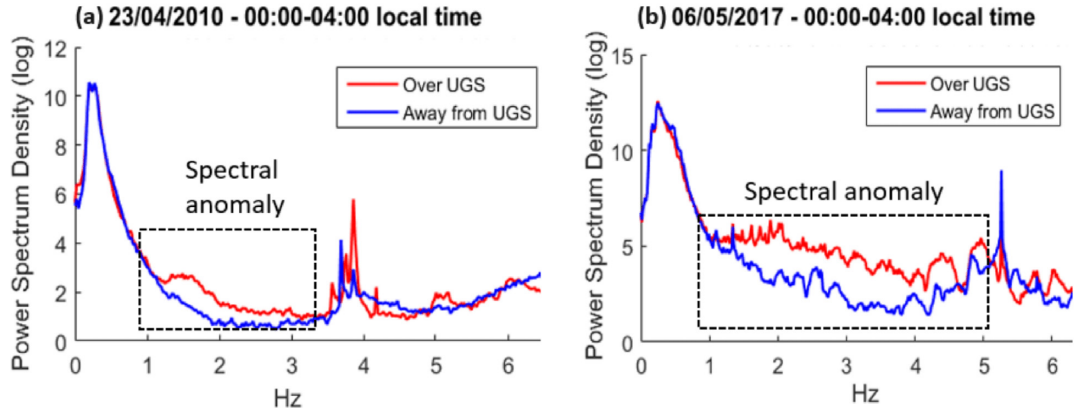

Figure 1. Vertical component power spectral density (PSD) recorded simultaneously above the UGS (red) and away from UGS (blue) on (a) Chémery site, (b) Saint-Illiers site (Kazantsev 2018).

either a true fluid signature in the ambient noise spectrum or a misinterpretation of the local noise sources and/or geological site effects. We refer to Kazantsev (2018) for a detailed literature review on this subject.

Fig. 1 shows an example of spectral anomalies observed on the vertical component at two underground gas storages (UGS) operated by Storengy in France. Kazantsev *et al.* (2019) investigated two possible mechanisms under pure elastic modelling in a 2-D context: (1) an effect of the local geological structure or (2) the presence of a hydrocarbon reservoir, leading to possible surface wave scattering and conversions. The conclusion, derived from a 2-D analysis, was that the geological structure (anticline), and not really the fluid reservoir, could be the main cause of the anomalies. For reasonable elastic parameters in the reservoir the predicted spectral anomaly was indeed 10 times lower than the real data anomalies.

Indeed, lateral heterogeneity in the subsurface can cause changes in the site response to ambient vibrations. It is characterized by altered material properties, or change in the geometry. For example, sedimentary valleys are a typical case of site amplification (2-D or 3-D resonance). Many studies covered this topic, and general laws relating the site response to the valley geometry and elastic properties were extracted (Bard & Bouchon 1985; Levander & Hill 1985; Steimen 2003). Opposite to U-shaped valleys, an anticline is a structural trap formed by the folding of rock strata into an arch-like shape. It is a typical characteristic of sites hosting hydrocarbon reservoirs and can be expected to cause changes to the site response. While it could be of primary interest for understanding the anomalies observed above hydrocarbon reservoirs, the effect of anticline structures on the ambient wavefield has not yet been studied in the literature, to our knowledge. Our objective is to relate the spectral anomalies observed at the surface to the geometrical characteristics of the anticline and the elastic properties of the background medium. Our work focuses on elastic propagation of wavefields dominated by surface waves, as they carry an important fraction of the ambient noise energy. We focus on Rayleigh waves rather than Love waves, because we aim to analyse the anomalies on the vertical component of the wavefield.

The first part of the paper provides a description of an approximate semi-analytical approach that we developed using the standard 1-D reflection–transmission matrix approach for surface waves. It is validated using the Spectral Element Method (SPECFEM3D software; Komatitsch & Vilotte 1998; Komatitsch *et al.* 1999) combined to the surface waves injection technique (Appendix A). In the second part, we use the semi-analytical approach to run a larger number of simulations to derive general characteristics of anticline-induced anomalies, and we perform some SEM simulations to assess the sensitivity of our results with respect to the source distribution.

2 APPROXIMATE SEMI-ANALYTICAL SURFACE WAVE MODELLING IN 3-D LATERALLY SMOOTHLY VARYING MODELS

In this part, we first recall a semi-analytical surface wave solution for a 1-D layered model (2.1). We then extend it to smoothly varying models. It mainly consists of combining local 1-D solutions at the source and receiver positions. The approach is validated with the Spectral Element Method. This tool will be the basis for our further analysis of the relationships between the anticline structure and the surface wave spectral anomalies (Section 3).

2.1 Semi-analytical surface wave 1-D modelling in laterally homogeneous media

We first indicate how to generate surface wave seismograms in a laterally homogeneous layered medium. Aki & Richards (2002) describe in details the solution for surface waves generated by a point force buried in a vertically heterogeneous medium. In the frequency domain, the displacement $u_i(\omega)$ for the component i, at a receiver with coordinates $\mathbf{x} = (x, y, z)$ is given by:

$$u_i(\mathbf{x}, \omega) = \sum_m \sum_j G_{ij}(\mathbf{x}, \omega) S_j(\omega), \tag{1}$$

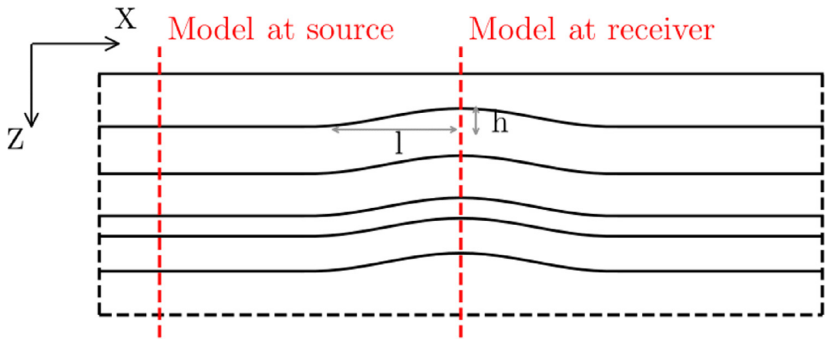

Figure 2. Description of the main geometrical characteristics of the model, as well as the source and receiver positions.

where ω is the angular frequency, m is the index of the surface wave mode, j is the index for source component, $S(\omega)$ of the source function and $G(\mathbf{x}, \omega)$ is the Green's tensor. For the case of Rayleigh waves the Green's tensor is given by eq. (7.147) in Aki & Richards (2002)

$$G^R = \frac{1}{8cuI_1}\begin{pmatrix} U_R(z)U_R(z_s)\cos\phi^2 & U_R(z)U_R(z_s)\cos\phi\sin\phi & -iU_R(z)U_Z(z_s)\cos\phi \\ U_R(z)U_R(z_s)\cos\phi\sin\phi & U_R(z)U_R(z_s)\sin\phi^2 & -iU_R(z)U_Z(z_s)\sin\phi \\ iU_Z(z)U_R(z_s)\cos\phi & iU_Z(z)U_R(z_s)\sin\phi & U_Z(z)U_Z(z_s) \end{pmatrix} \times\sqrt{\frac{2}{\pi k_n r}}\exp\left[-ik_n r+\frac{\pi}{4}\right], \tag{2}$$

where $c = c(\omega)$ and $u = u(\omega)$ are the phase and group velocity, respectively, $U_R = U_R(z, \omega)$ and $U_Z = U_Z(z, \omega)$ are the displacement eigenfunctions in the radial and vertical directions, respectively, z_s is the source z-coordinate, $\phi = \phi(x, y)$ and $r = r(x, y)$ are respectively the angle and the distance between the source and the receiver in the horizontal plane and $k_n = \omega/c(\omega)$ is the wavenumber. I_1 is the energy integral given by by eq. (7.74) in Aki & Richards (2002)

$$I_1 = \frac{1}{2}\int_0^\infty \rho\left(U_R^2 + U_Z^2\right)\mathrm{d}z, \tag{3}$$

with ρ the medium density. All the previous quantities are specific to the mode m in the sum.

Displacement eigenfunctions U_R and U_Z and the phase and group velocities c and U are calculated using the CPS codes (*Computer Programs for Seismology*) developed by Herrmann (2013). We call the method *semi-analytical* because this calculation requires a numerical resolution of a linear system of equations.

We then compute the Green's tensor terms and we sum over sources and modes in the frequency domain. After summation, we transform the total output to the time domain using the inverse Fourier transform to get synthetic displacement and traction seismograms.

2.2 Approximate solution for smooth laterally heterogeneous media

For models containing smooth lateral variations, such as an anticline, we propose an extension referred to as the *approximate* semi-analytical surface wave modelling. Following Woodhouse (1974), in the case of slowly varying structures, the concept of local modes is used. Local modes are surface waves modes that propagate in a fictitious laterally homogeneous model behaving as a 1-D model at each considered location. Gualtieri *et al.* (2015) use local modes to study the effect of the ocean depth on Rayleigh waves generated by sources in deep and in shallow water. The authors generate synthetic seismograms by local mode superposition, by multiplying the eigenfunction relative to the 1-D medium at the source location by the eigenfunction computed in the 1-D medium at the receiver location. We follow the same philosophy here.

We consider the anticline structure as a slowly laterally varying structure if the h/l ratio is relatively small, with h the height of the anticline and l its half-width (Fig. 2). The 1-D model at the source location is the reference laterally homogeneous model far from the anticline, and the 1-D model at the receiver location is a section of the model passing through the anticline top (Fig. 2). The model at the receiver location has the same layer properties and same layer thicknesses as the model at the source location except for the surface layer that has a reduced thickness compared to the model at the source. The model at the receiver is a shifted version of the model at the source caused by the thinning of the shallow layer. In order to obtain synthetic seismograms representing the propagation of surface waves between the two 1-D models, we make the following modifications in the Green's tensor (eq. 2) introduced in Section 2.1: $U_R(z_s) \rightarrow U_{Rs}(z_s)$, $U_Z(z_s) \rightarrow U_{Zs}(z_s)$, $U_R(z) \rightarrow U_{Rr}(z)$, $U_Z(z) \rightarrow U_{Zr}(z)$, $I_1 \rightarrow \sqrt{I_{1s}I_{1r}}$, $c \rightarrow \sqrt{c_s c_r}$, $U \rightarrow \sqrt{u_s u_r}$ and $k_n \rightarrow \sqrt{k_{ns}k_{nr}}$. This is a simple way to consider the lateral variability.

Table 1. Properties of the three-layer models used for simulations.

model 1				
Layers	Thickness (m)	ρ (kg m^{-3})	v_P (m s^{-1})	v_S (m s^{-1})
L1	400	1500	1800	1000
L2	320	1850	2600	1450
L3	–	2500	4000	2200
model 2				
Layers	Thickness (m)	ρ (kg m^{-3})	v_P (m s^{-1})	v_S (m s^{-1})
L1	400	1400	1300	650
L2	320	2000	3000	1500
L3	–	3000	5000	2500

2.2.1 Validation

To validate the accuracy of this method, we compare the outputs with a 3-D spectral-element simulation combined with the surface waves injection technique (Appendix A). The validation is performed for the case of Rayleigh waves and separately for each Rayleigh wave mode. The analytical solution for Rayleigh waves in the reference 1-D model is injected in SPECFEM3D at the boundaries of a small 3-D model containing the anticline structure. The 1-D model properties are listed in Table 1 (model 1). Source positions are distributed uniformly around the model. Simulations are performed taking different h and l dimensions. Once the seismograms at the surface are computed, we calculate the power spectral densities on the vertical component at a point (x_i, y_i) by

$$\mathrm{PSD}_Z(x_i, y_i, \omega) = |\mathrm{FFT}(v_Z(x_i, y_i, t))|^2, \tag{4}$$

where we omit the normalization constant for simplicity. We then calculate an attribute p, in decibels, that can be interpreted as the anticline-induced spectral anomaly:

$$p(x_i, y_i, \omega) = 10 \log_{10} \left(\frac{\mathrm{PSD}_{Z,\mathrm{anticline}}(x_i, y_i, \omega)}{\mathrm{PSD}_{Z,\mathrm{plane}}(x_i, y_i, \omega)} \right). \tag{5}$$

$\mathrm{PSD}_{Z,\,\mathrm{plane}}$ is calculated in the reference model free of any lateral heterogeneity.

On the other hand, using the approximate semi-analytical approach (eqs 2 and 4), $\mathrm{PSD}_{Z,\,\mathrm{plane}}$ is proportional to $(1/\sqrt{c_s} u_s I_{1s}))^2$ and $\mathrm{PSD}_{Z,\,\mathrm{anticline}}$ amplitude is proportional to $(1/(\sqrt{c_s} u_s I_{1s})) \times (1/(\sqrt{c_r} u_r I_{1r}))$. Thus the anomaly p can be written as:

$$p(\omega) = 10 \log_{10} \left(\sqrt{\frac{c_s(\omega)}{c_r(\omega)}} \frac{u_s(\omega)}{u_r(\omega)} \frac{I_{1s}(\omega)}{I_{1r}(\omega)} \right). \tag{6}$$

The p anomaly is computed for a line of stations along the X direction passing by the centre of the anticline, and maps of the attribute p as function of in-line distance and frequency are plotted. Fig. 3 compares the anomalies resulting from the analytical and 3-D numerical simulations, for the fundamental mode of Rayleigh waves, in models having different anticline half-widths and heights.

We observe a clear similarity in shape and amplitude of the spectral anomalies between both methods, except for small values of l (200 m) where the approximate semi-analytical approach overestimates the anomaly amplitudes. The reason can be that the heterogeneity became very small and acts as a diffraction point for the wave with a wavelength significantly larger than the heterogeneity, violating the 1-D model assumption. By construction the amplification computed by the semi-analytical approach is independent of the width of the anticline. This confirms that the method proposed here is only accurate for slowly laterally varying structures. In real cases discussed in Kazantsev (2018), this condition is satisfied in the frequency range of interest (1 to several Hz). A first conclusion is that the amplitudes of the anomalies are larger for larger values of h, that is more prominent anticline shape. This aspect is further generalized in Section 3.2.2.

In addition, the comparison between analytical and numerical modelling is only satisfactory for the case of a uniform azimuthal source distribution. In the case of non-uniform azimuthal distributions, the shape of the anomaly is strongly influenced by the sources azimuths. This limitation is illustrated in Section 3. In real data it is common to find one or several dominant azimuths of sources, usually of finite azimuthal width.

Consequently, this method is only intended to be used as a first reference for a fast estimation of 1-D anomaly amplitudes and characteristic frequencies above the central part of the anticline structure (Section 3.2.2). In practice and under some restrictions, the approximate semi-analytical method is useful because it allows performing a very large number of tests with varying many parameters within a short computational time. This would be prohibitive with full 3-D numerical simulations. A simulation that lasts six hours for a full 3-D simulation using a large SPECFEM3D model, is reduced to one hour when combined with the injection technique on a smaller model (Appendix A2), and costs nearly 1 min using the approximate semi-analytical solution. Our method will be used in Section 3.2.2 to get the general shape of spectral anomalies caused by an anticline structure in a model dominated by fundamental mode Rayleigh waves. We will vary independently the prominence (height of the anticline) and the elastic properties of the surface layer.

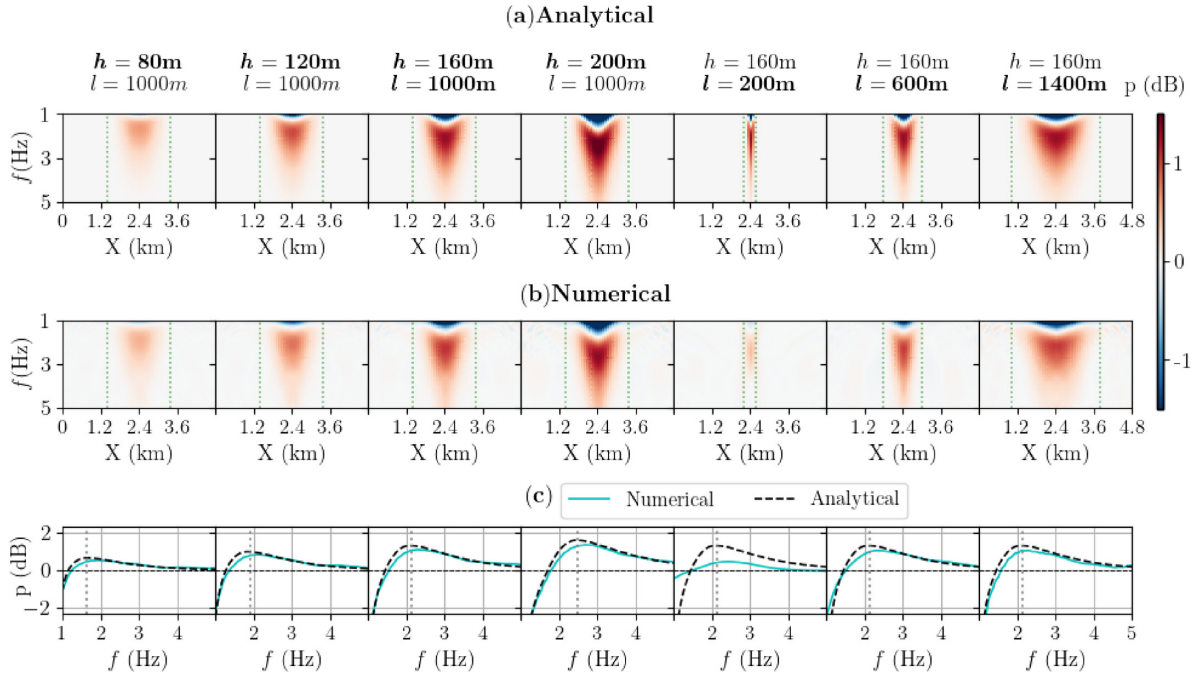

Figure 3. Simulated anticline-induced amplitude anomalies at a line of stations passing by the anticline (at $Y = 2.4$ km), compared between (a) analytical and (b) 3-D numerical simulations using uniformly distributed sources along azimuths for different values of h and l. The dotted vertical green lines correspond to the lateral limits of the anticline. (c) Simulated anticline-induced amplitude anomalies at the central station ($X = 2.4$ km, $Y = 2.4$ km) compared for both methods. The dotted grey lines correspond to the frequency where the maximum positive analytical anomaly occurs.

3 MODELLING RESULTS: EFFECT OF AN ANTICLINE STRUCTURE

In this part, we present the results of simulations that we conducted to study and better understand the spectral anomalies on the Rayleigh waves vertical components generated by the presence of an anticline structure.

To generate Rayleigh waves in a 3-D model, sources must be located far from the zone of interest. In spectral-element simulations with sources located inside the 3-D model we would be constrained to use a model of large dimensions to generate a wavefield dominated by surface waves. A point source within the model inevitably generates a mixture of modes, so depending on the depth of the source in the medium, we get more dominance of fundamental mode or higher modes of Rayleigh waves. By using the 1-D analytical solution for surface waves and surface waves injection technique (Appendix A2), we were able to conduct a high number of simulations as well as to study the effect of each Rayleigh wave mode separately.

3.1 Source wavefield from one direction

The first simulations are performed in a simplified three layer model. The 1-D analytical solution for the fundamental mode of Rayleigh waves is injected on the boundaries of a smaller SPECFEM3D model of dimensions 4.8 km × 4.8 km × 1.04 km. The anticline structure is modelled as a 3-D sine shaped deformation of the interfaces (Fig. 4b). The anticline height is $h = 160$ m and its half-width is $l = 1000$ m. In the first simulation, we use one Ricker wavelet source of central frequency 1.5 Hz, located at $X = -10$ km and $Y = 2.4$ km, at the surface. Note also that the source is located outside the small 3-D model and the wavefield is propagated analytically from the source to the model boundaries.

Using model 2 (Table 1), vertical displacement snapshots on a vertical plane XZ crossing the anticline top and on the surface plane XY are plotted in Fig. 4. Before reaching the heterogeneity, one wavelength dominates the wavefield. The corresponding frequency is expected to be close to the vertical resonance frequency $f_{0P} = v_{P1}/4h_1$ (Parolai & Richwalski 2004), with v_{P1} the P-wave velocity in the shallow layer and h_1 the thickness of the surface layer. Upon reaching the heterogeneity, we observe a divergence of the wavefield. In the XY plane snapshot (Fig. 4a) and in the horizontal direction downstream the anticline, the amplitude is attenuated (defocusing effect) but new frequencies are dominating, as already noticed in the XZ plane. At diagonal directions superposition of the diverging wave and the incident wave occurs, creating higher amplitudes (focusing effect).

We used model 2 (Table 1), that presents a high contrast between the surface layer and the second layer, only for plotting the displacement snapshots in Fig. 4, in order to better visualize the (de)focusing effect. In the following parts, we will present the results of simulations with model 1, which has a lower contrast. For model 1, we choose elastic properties which are typical for the velocity models based on reflection

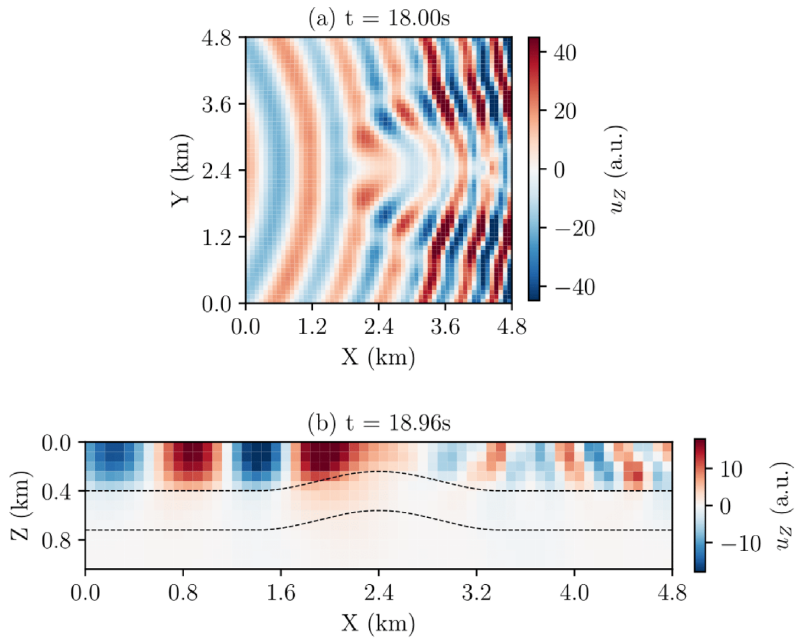

Figure 4. Vertical displacement snapshots computed for model 2 (Table 1) at the surface (a), and along a vertical cross-section passing by the anticline (b). The two snapshot captures are slightly delayed ($\sim$ 1 s) in order to visually capture the important features of the wavefield in both projections.

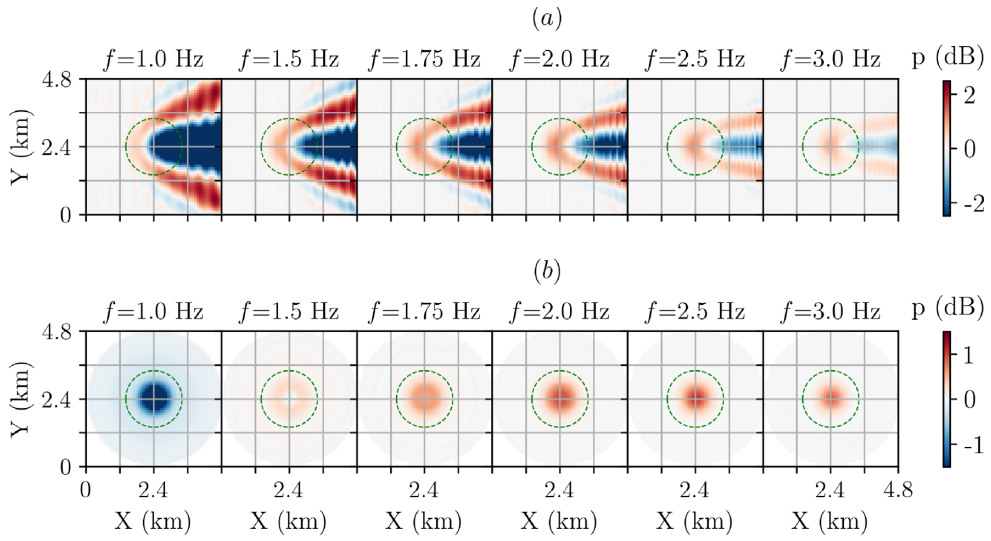

Figure 5. Anticline-induced anomaly (attribute p) computed for model 1 maps at the surface for different frequencies, computed for (a) a single-azimuth source by numerical 3-D simulation (R0 waves injection with sources located at $X = -9$ km and $Y = 2.4$ km), (b) uniformly distributed sources along the azimuths.

seismic surveys and sonic logs recorded in boreholes. The width and height of the anticline are also typical for underground gas storage reservoirs operated by Storengy.

To quantitatively illustrate the effect of the anticline structure, we calculate the PSD_Z at each station of the surface (eq. 4). We compare the results with a simulation in a laterally invariant model by calculating the attribute p (eq. 5), yielding the relative anomaly in Decibel. Using the same source located at $X = -9$ km and $Y = 2.4$ km, we plot the attribute p for model 2 (Table 1) at different frequencies and at each position at the surface (Fig. 5a). The source location signature is very clear: stations downstream the anticline present negative anomalies due to the defocusing effect. On either sides of this negative anomaly, focusing is observed, creating a positive anomaly. These features were already visible in the wavefield snapshots in Fig. 4, as previously stated. Such a 3-D effect cannot be visible in 1-D or 2-D XZ modelling (Kazantsev *et al.* 2019). The station located exactly above the top of the anticline ($X = 2.4$ km, $Y = 2.4$ km), presents a negative anomaly at low frequency followed by a positive anomaly starting approximately at 1.5 Hz.

3.2 Source wavefield from all directions

3.2.1 3-D simulations

The second case study is performed with sources having a uniform azimuthal distribution. In this case, individual source azimuth signatures through (de)focusing are expected to cancel out leaving place to the pure anticline signature.

If we consider uncorrelated sources in time, the contributions of sources in terms of power spectral density can be directly summed. Having a symmetrical 3-D model with respect to a vertical axis passing by the central station, a change in the source azimuth results in a rotation of the PSD_Z maps, so we do not need to repeat the 3-D simulation for different source azimuths. We consider here 36 sources distributed uniformly along the azimuths (1 source every 10°), we sum their contributions in terms of PSD_Z, and we calculate the resulting anomaly p at each station of the surface.

We plot the anomalies at the surface for different frequency values (Fig. 5b). The contribution of each individual source is similar to the one described in the previous part. The total anomaly appears as the sum of all the contributions, as far as the sources are uncorrelated. Inside the zone of the anticline, at $f = 1.0$ Hz, a negative anomaly dominates and at $f > 1.0$ Hz, a positive anomaly accumulates. Outside the zone of the anticline, positive and negative zones are of equivalent size in the individual contributions, so the total anomaly becomes negligible. We conclude that for the case of fundamental mode of Rayleigh waves, we expect to have a negative anomaly at low frequency followed by a positive anomaly for a large frequency range at a station located on the top of the anticline. The frequency limit between the negative and the positive anomaly (here between 1 and 1.5 Hz) varies for different models and for different shapes of the anticline. The shape of the anomaly and its variation will be studied in the next paragraph.

In real data, sources originate from specific azimuths or range of azimuths. So a uniform distribution of sources may not be representative. On the other hand, the (de)focusing pattern observed in the case of a single azimuth source is not clearly visible in real data and the anomaly is mostly concentrated in the anticline zone. In Appendix B, we present results of the anticline-induced anomalies obtained with 3-D spectral element simulations with different source combinations. For some realistic source combinations, we are able to reduce the (de)focusing pattern outside the anticline zone.

3.2.2 1-D simulations: deriving a general anomaly shape

We study here the variation of the shape of the anomaly spectrum with respect to different geometrical and elastic parameters, for the case of the fundamental mode of Rayleigh waves. We use the approximate semi-analytical approach (section 2.2) because we need to perform a very large number of simulations and we are now only interested in the anomaly spectrum located at the top of the anticline. The presence of an anticline is fully described by a decrease in the surface layer thickness. The surface layer thickness in the 1-D model at the source is h_1, and $h_1 - h$ at the receiver, h being the anticline height.

We start by studying a model containing a single layer over an infinite half-space. The parameters that we vary simultaneously are:

We will first transform eq. (10), which yields the anomaly spectrum, to a more convenient shape. Under fixed elastic parameters, there is a dimensionless frequency $f^* = Hf/\beta_1$ for group and phase velocities, so that their shapes do not depend on the thickness of the first layer (Mooney & Bolt 1966). The group and phase velocities can be written as $u(H, f) = u^*(f^*)$ and $c(H, f) = c^*(f^*)$. For the term I_1, not treated by Mooney & Bolt (1966), we introduce the dimensionless depth $z^* = z/H$, so that the eigenfunctions U_R and U_Z have a unique shape completely determined by f^* and z^*. Substituting into eq. (3) we get $I_1(H, f) = H I_1^*(f^*)$. In Fig. 6 we show that $c(f)/\beta_1$, $u(f)/\beta_1$ and $I_1(f)/(\rho_1 H)$, plotted for different values of surface layer thickness H, collapse into one curve after converting the physical frequency in Hz into the dimensionless frequency f^*. Substituting these dimensionless frequency functions in eq. (6), and using the dimensionless frequency of the 1-D model at the source ($f^* = h_1 f/\beta_1$), the anomaly p can be written as function of γ and f^* only:

$$p(\gamma, f^*) = 10 \log_{10} \left(\frac{1}{\gamma} \sqrt{\frac{c_s^*(f^*)}{c_r^*(\gamma f^*)}} \frac{u_s^*(f^*)}{u_r^*(\gamma f^*)} \frac{I_{1s}^*(f^*)}{I_{1r}^*(\gamma f^*)} \right). \tag{7}$$

We plot the anomaly p as function of γf^* for a model M1 with elastic properties defined in Table 2 and for different anticline prominence γ (Fig. 7a). The global shape of the anomaly presents similarities for all values of γ. By increasing γ we get higher values of anomaly, and the positive anomaly occurs at a slightly higher f^*.

From the dimensionless eq. (7), we are going to study how the anomaly maximum value $p_{\max}$ and the associated frequency $f^*_{\max}$ vary with γ and the elastic parameters of the background medium. The purpose is to obtain even simpler empirical laws which do not require the evaluation of the Rayleigh wave eigenfunctions and phase and group velocities. These dependencies are illustrated in Fig. 7(b) for four models with different elastic properties and the full range of γ.

After exploring a large number of parameter combinations, we find that the shape of $p_{\max}$ as function of γ can be approximated by a polynomial of degree 4 in γ for any value of elastic parameters. We also find that we can further impose $p_{\max}(1) = 0$, $p'_{\max}(0) = 0$ and $p''_{\max}(0) = 0$ without loss of generality:

$$\tilde{p}_{\max}(\gamma, \sigma_1, \rho_1/\rho_2, \beta_1/\beta_2) = a_0 + a_1\gamma^3 - (a_0 + a_1)\gamma^4. \tag{8}$$

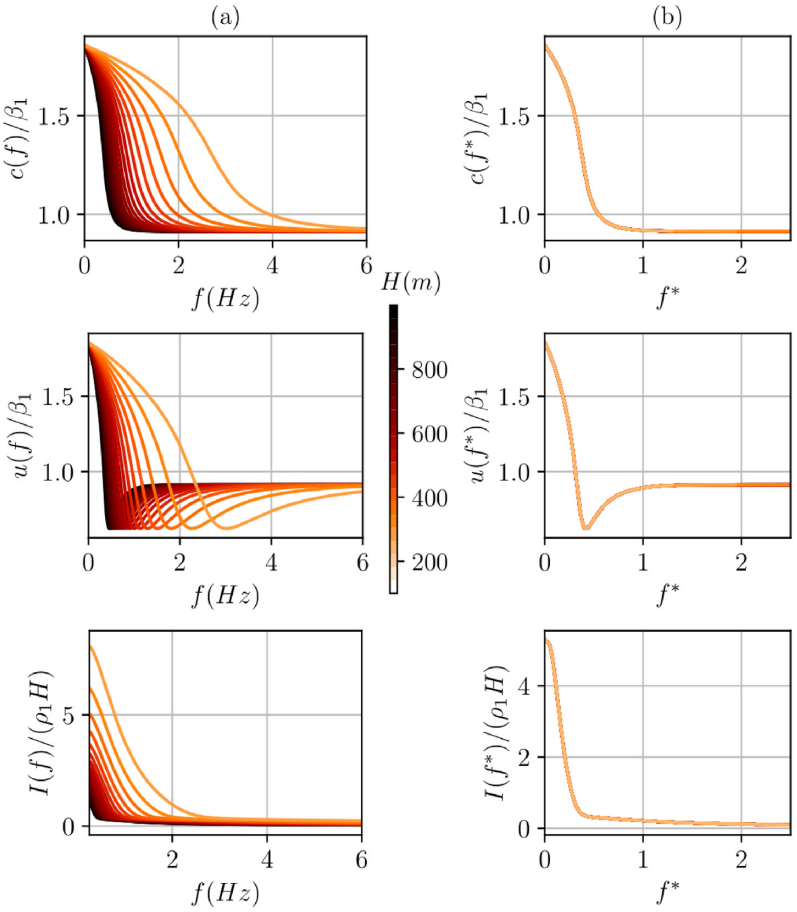

Figure 6. Phase velocity, group velocity and energy integral I for different values of surface layer thickness H with respect to (a) frequency, (b) dimensionless frequency f^* (curves are superposed).

Table 2. Elastic properties for four two-layer models.

Models	σ_1	ρ_1/ρ_2	β_1/β_2
M1	0.22	0.9	0.5
M2	0.18	0.4	0.8
M3	0.38	0.8	0.4
M4	0.31	0.5	0.5

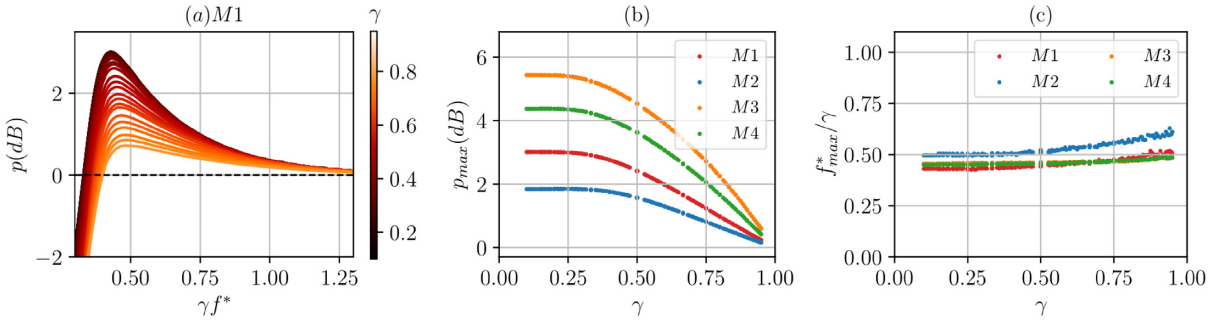

Figure 7. (a) Anomaly p with respect to γf^* for a model M1 with fixed elastic properties, for different values of the geometry factor γ. (b) Amplitudes of the positive anomaly peaks with respect to γ for four models with different elastic properties (Table 2). (c) γ multiplied by the dimensionless frequency of the positive anomaly peaks with respect to γ for the four models.

Table 3. Coefficients resulting from the approximations of a_0 and a_1.

b_{ijk}	b_{000}	b_{100}	b_{001}	b_{002}	b_{110}	b_{011}	b_{003}	b_{102}	b_{012}	b_{111}
a_0	−5.24	−5.45	9	−3.62	6.25	−0.925	0.39	2.21	0.23	−2.1
a_1	28.33	0	−45.35	19.35	0	0	−2.72	0	−2.89	0

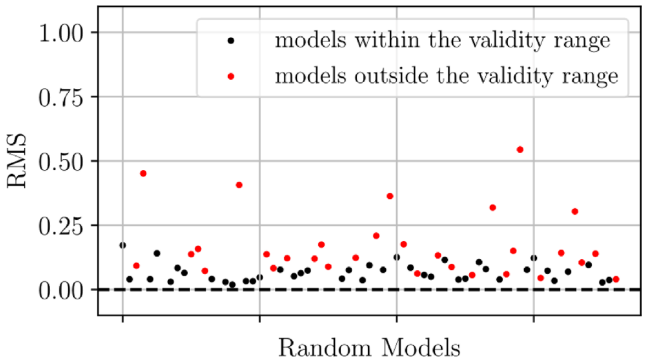

Figure 8. RMS resulting from approximation of the maximum anomaly $p_{\max}$ on models with random elastic properties (not used in the model optimization).

Coefficients a_0 and a_1 carry the dependence in the elastic parameters. From a qualitative point of view, the elastic parameter that has the biggest influence is the *S*-wave velocity contrast (β_1/β_2). For higher contrasts we reach higher anomaly peak values (Fig. 7b). However we should not exclude the influence of the density ratio (ρ_1/ρ_2) and the Poisson ration of surface layer (σ_1). Mathematically, a_0 and a_1 can be approximated as a function of the three elastic parameters by:

$$\tilde{a}_m(\sigma_1, \rho_1/\rho_2, \beta_1/\beta_2) = \sum_i^{n_i} \sum_j^{n_j} \sum_k^{n_k} b_{i,j,k,m} (\sigma_1)^i (\rho_1/\rho_2)^j (\beta_1/\beta_2)^{-k}, m \in 0, 1, \tag{9}$$

where $n_{i,j,k}$ are the polynomial orders of the approximation in the three elastic parameters. We perform optimization of the coefficients $b_{i,j,k,m}$ based on a set of models sampled regularly in the 3-D corresponding to the three elastic parameters. The resulting optimal coefficients $b_{i,j,k,m}$ are listed in Table 3, where we omit some coefficients that have negligible influence on the quality of the approximation. This approximation seems good for fairly wide parameter validity ranges. There are few combinations of parameters for which the fit is poor, for example a model with a large σ_1 and low β_1/β_2. The final validity range with acceptable fit is:

$$\begin{aligned} 0.3 \leq \beta_1/\beta_2 \leq 0.9 \\ 0.3 \leq \rho_1/\rho_2 \leq 0.9 \\ 0.1 \leq \sigma_1 \leq 0.45 \\ \sigma_1(\beta_1/\beta_2)^{-1} \leq 0.7 \end{aligned} \tag{10}$$

After having determined the optimal coefficients on a regular grid, we test the optimal set of coefficients on other random models to check the prediction capacity of our approximation. In Fig. 8 we show the final RMS error of our approximated prediction (eqs 8 and 9) with respect to the 'correct' $p_{\max}$ computed with eq. (7). The approximation is satisfying (values of RMS mostly below 0.15) for random models chosen within the validity range.

We are now interested by the frequency $f^*_{\max}$ of the positive anomaly peak (Fig. 7c). We define $C = \gamma\ f^*_{\max}$. From the definition of the dimensionless frequency f^*, the frequency of the true maximum anomaly in Hz can be written as $f_{\max} = C\beta_1/(h_1 - h)$. C ranges between 0.4 and 0.65 approximately and we assume that it is a linear function of γ (Fig. 7c). The values of C are mostly influenced by the velocity contrast between first and second layer (β_1/β_2). An approximated equation of C is given by:

$$\tilde{C} = \gamma\, \tilde{f}^*_{\max}(\gamma, \beta_1/\beta_2) = 0.33 + 0.16(\beta_1/\beta_2) + 0.22(\beta_1/\beta_2)\gamma. \tag{11}$$

Using the maximum anomaly approximation (eqs 8 and 9), we fix the values of two parameters and plot the variation of $\tilde{p}_{\max}$ as function of the other two parameters (Fig. 9). We confirm here that the anomalies are higher for a higher prominence of the anticline (higher γ), a higher Poisson ratio σ_1, a higher density contrast (lower ρ_1/ρ_2) and a higher *S*-velocity contrast (lower β_1/β_2). Among the three elastic parameters, the *S*-velocity contrast has the highest influence on the anomaly values. In real data, the anomalies could show fluctuations of a few decibels due to other effects not taken into account here. Thus, for fixed parameters, one can determine a threshold above which we can relate the anomalies to anticline-induced anomalies. In our case (Fig. 9), if we consider a threshold of 2 dB and a shape ratio $\gamma = 0.5$, the anomaly related to the anticline structure becomes visible for a *S*-velocity ratio below 0.7 (Fig. 9c).

By knowing the elastic properties (σ_1, ρ_1/ρ_2, β_1/β_2) and the surface layer thickness (h_1) as well as the height of the anticline (h), we were able to get a rapid estimation (before any simulation) of the amplitude and the characteristic frequency of the anomaly generated by the presence of the anticline structure at a location directly above the anticline centre, for the case of a wavefield dominated by fundamental

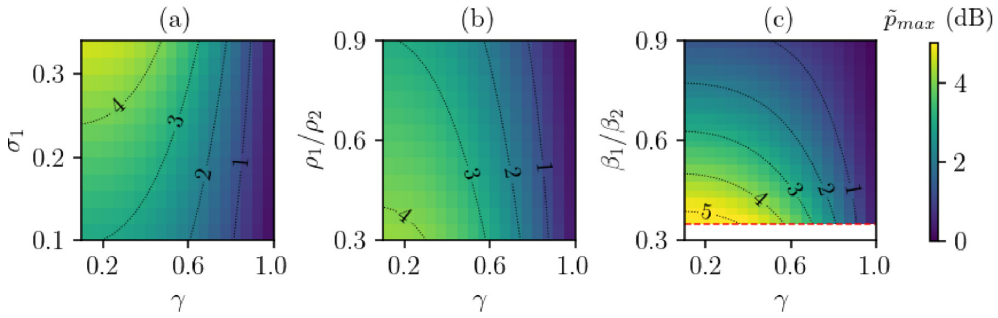

Figure 9. $\tilde{p}_{\max}$ variation as function of two parameters: (a) σ_1 and γ, (b) ρ_1/ρ_2 and γ, (c) β_1/β_2 and γ, the two remaining elastic parameter being fixed in each plot ($\sigma_1 = 0.24$, $\rho_1/\rho_2 = 0.4$, $\beta_1/\beta_2 = 0.5$). The black dotted lines are contour lines of $\tilde{p}_{\max}$ and the red dashed line in (c) represents the limit of the validity range in the $\tilde{p}_{\max}$ approximation (eq. 10).

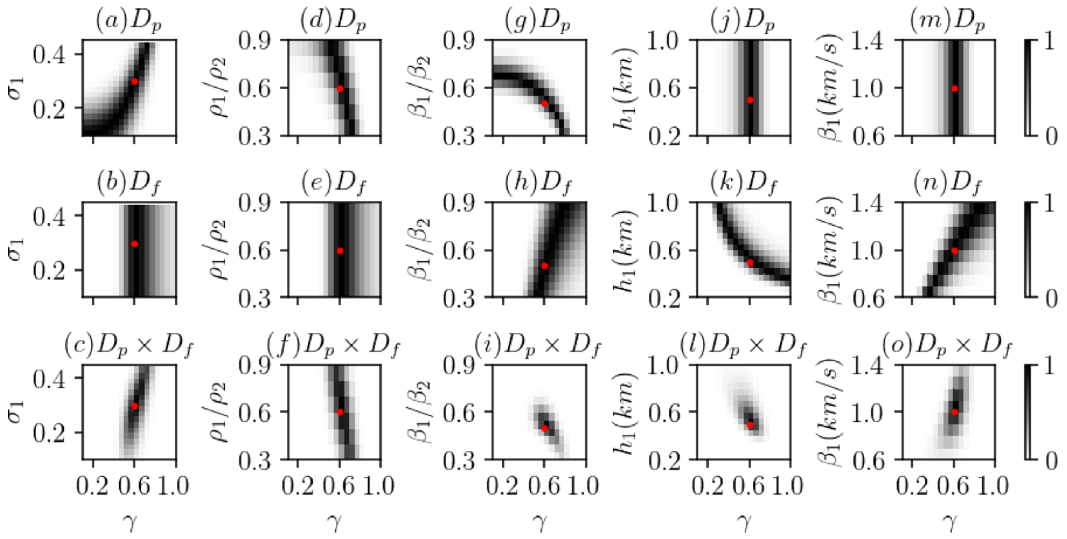

Figure 10. Variation of D_p, D_f and $D_p \times D_f$ as function of two parameters in each case. The red dot corresponds to the properties of the reference model M_{ref}.

mode Rayleigh waves. Although a formal extension to multilayered models still needs to be developed, first results showed that the global shape of the anomaly is preserved with small variations in amplitude due to the influence of the deep layers. Reciprocally, in real data sets, one can extract the anomaly peak amplitude and frequency, $p_{\max,\,\text{obs}}$ and $f_{\max,\,\text{obs}}$. Knowing two parameters among σ_1, ρ_1/ρ_2, β_1/β_2 and γ, we can find a relationship between the two remaining parameters using eqs (8) and (11). Here we should add two additional variables, h_1 and β_1, to be able to transform the physical frequency $f_{\max}$ into the dimensionless frequency $f^*_{\max}$. To illustrate this, we choose a model M_{ref} having parameters that give $\tilde{p}_{\max} = p_{\max,\text{obs}}$ and $\tilde{f}_{\max} = f_{\max,\text{obs}}$. We calculate the density functions:

$$D_p = e^{-\frac{1}{2}\frac{|\tilde{p}_{\max} - p_{\max,\text{obs}}|^2}{s_{\tilde{p}}^2}} \tag{12}$$

$$D_f = e^{-\frac{1}{2}\frac{|\tilde{f}_{\max} - f_{\max,\text{obs}}|^2}{s_{\tilde{f}}^2}}, \tag{13}$$

with $s_p = 0.5$ and $s_f = 0.25$. If $\tilde{p}_{\max} = p_{\max,\text{obs}}$ and $\tilde{f}_{\max} = f_{\max,\text{obs}}$, then $D_p = 1$ then $D_f = 1$.

In Fig. 10, we plot D_p, D_f and $D_p \times D_f$, each time fixing two parameters and varying the others on a regular grid. The method shows good prediction capacity especially when predicting the geometry factor or the prominence of the anticline structure γ from the shear wave velocity contrast β_1/β_2, from the surface layer thickness h_1, from the surface layer shear wave velocity and vice versa (Figs 10i,l,o). This makes our method useful for applications such as the ambient noise tomography as it adds a constraint to the problem. However direct predictions from real data sets is not yet accurate because our method is valid for a uniform azimuthal distribution of sources and for 2-layer media. We should either extend it to multilayered media or consider an effective half-space with effective thickness of surface layer h_1 and effective elastic properties. For a multilayered model, an alternative is to calculate the phase and group velocities and the energy integral of two models (one at the source and the other at the receiver) and to calculate the anomalies applying directly eq. (6). Then we extract the maximum anomaly and the corresponding frequency peak without the use of approximated formulae.

4 DISCUSSION

In this work, we were able to show that the presence of an anticline could be a good candidate to explain the amplitude anomalies often observed above hydrocarbon fields. Our results suggest that the anticline-induced anomaly shape, for the case of a wavefield dominated by the fundamental mode of Rayleigh waves, is characterized by a negative anomaly followed by a positive anomaly in a large frequency range.

However, in real data, the negative anomaly is usually not detected. One explanation could be that in our real data sets fundamental mode Rayleigh waves are not dominant in the frequency range where the negative anomaly would be expected (typically between 0.5 and 1 Hz). We plan to make a detailed study of the noise composition on real data sets in a separate paper. Another aspect regarding the (de)focusing pattern, usually not as visible in real data sets as in our simulations (see Fig. A6), is to study if it remains stable in simulations performed in a scattering medium, in particular where the coherency length is smaller than the anticline width.

On the other hand, the analysis of the shape of anomalies computed with the approximate semi-analytical method is limited to the case of an omnidirectional wavefield. However in real data, sources originate from specific azimuths. The wave (de)focusing caused by the interaction with the anticline structure is not taken into account with this method in its current state. Thus the approximate semi-analytical approach should be only used as a rule of thumb for a fast estimation.

Future studies with the approximate-analytical approach could include the case of multilayered media and the case where the anticline shape affects deeper layers, leaving an non-deformed surface layer, with the aim of finding how the anomalies could be affected. Concerning the Rayleigh wave first overtone, few tests were done to try to find a shape for anomalies. However, the shape of the anomalies generated by the mode R1 is complicated and varies a lot from one model to another, mainly because the R1 eigenfunctions are not a simple uniformly decreasing function of depth, which gives rise to a variety of possible behaviours.

5 CONCLUSION

This work is part of investigating the nature of the ambient noise spectral anomalies observed above some hydrocarbon fields. We focused on modelling the effect of an anticline structure on the vertical component spectral amplitude of seismic ambient noise. Our two basic assumptions are that (1) the presence of an anticline is a common geological feature to many hydrocarbon fields, and (2) that the vertical component of seismic ambient noise is mostly dominated by Rayleigh waves. We used 3-D spectral-element modelling coupled with surface wave injection at the boundaries to account for both source distribution and anticline effects. It shows that sources located at one particular azimuth leave their signature in the amplitude anomaly spatial distribution via (de)focusing on the anticline, which leads to relatively complex anomaly patterns. When having sources uniformly distributed along the azimuths, the (de)focusing effect is not visible. In this case, the spectral anomaly induced by the anticline takes a relatively simple shape for the fundamental Rayleigh mode. This shape exhibits a negative anomaly at low frequency followed by a positive anomaly at high frequency. The positive anomaly can exceed a factor of 2. We were able to confirm this anomaly shape using a computationally efficient semi-analytical approach based on the local-mode approximation and classical 1-D calculations for surface waves in layered media. A large number of simulations performed for various anticline geometries and surface layer elastic properties allowed us to derive a general law for the positive anomaly maximum amplitude as well as the associated frequency. Future works will include simulations on realistic velocity models for real underground gas storage sites as well as a detailed analysis of real data ambient noise measurements over a long period on such sites. The objective is to compare the measured spectral anomalies with numerical modelling to be able to conclude if the former can be fully explained by the presence of an anticline structure, or if the ambient noise amplitude might still present some potential for reservoir monitoring/exploration.

ACKNOWLEDGMENTS

The authors thank Storengy for funding the project and granting access to the data and their presentation.

DATA AVAILABILITY

Due to confidentiality agreements, supporting data cannot be made openly available.

REFERENCES

Aki, K. & Richards, P.G., 2002. *Quantitative Seismology,* University Science Books.

Bard, P.-Y. & Bouchon, M., 1985. The two-dimensional resonance of sediment-filled valleys, *Bull. seism. Soc. Am.,* **75,** 519–541.

Beller, S., 2017. *Imagerie lithosphérique par inversion de formes d'ondes télésismiques – Application aux Alpes Occidentales,* Ph.D. thesis, Université Côte d'Azur.

Berenger, J.-P., 1994. A perfectly matched layer for the absorption of electromagnetic waves, *J. Comput. Phys.,* **114**(2), 185–200.

Bonnefoy-Claudet, S., Cotton, F. & Bard, P.-Y., 2006. The nature of noise wavefield and its applications for site effects studies, *Earth-Sci. Rev.,* **79**(3–4), 205–227.

Chaljub, E., Komatitsch, D., Vilotte, J.-P., Capdeville, Y., Valette, B. & Festa, G., 2007. Spectral-element analysis in seismology, *Adv. Geophys.,* **48,** 365–419.

Clayton, R. & Engquist, B., 1977. Absorbing boundary conditions for acoustic and elastic wave equations, *Bull. seism. Soc. Am.,* **67**(6), 1529–1540.

Dangel, S., Schaepman, M.E., Stoll, E.P., Carniel, R., Barzandji, O., Rode, E.D. & Singer, J.M., 2003. Phenomenology of tremor-like signals observed over hydrocarbon reservoirs, *J. Volcanol. Geotherm. Res.,* **128**(1), 135–158.

Gualtieri, L., Stutzmann, E., Capdeville, Y., Farra, V., Mangeney, A. & Morelli, A., 2015. On the shaping factors of the secondary microseismic wavefield, *J. geophys. Res.: Solid Earth,* **120**(9), 6241–6262.

Hanssen, P. & Bussat, S., 2008. Pitfalls in the analysis of low frequency passive seismic data, *First Break,* **26,** 111–119.

Herrmann, R.B., 2013. Computer programs in seismology: an evolving tool for instruction and research, *Seismol. Res. Lett.,* **84**(6), 1081–1088.

Holzner, R., Eschle, P., Dangel, S., Frehner, M., Narayanan, C. & Lakehal, D., 2009. Hydrocarbon microtremors interpreted as nonlinear oscillations driven by oceanic background waves, *Commun. Nonlinear Sci. Numer. Simul.,* **14**(1), 160–173.

Kazantsev, A., 2018. *Ambient noise spectral amplitude distortions above heterogeneities: feasability study for multi-fluid reservoir exploration and monitoring,* Ph.D. thesis, MINES ParisTech - Université de recherche Paris Sciences et Lettres PSL Research University, Paris, France.

Kazantsev, A., Chauris, H., Dublanchet, P. & Huguet, F., 2019. Rayleigh wave amplitude distortions above a reservoir: new insights from elastic modelling, *Geophys. J. Int.,* **217**(2), 1267–1289.

Komatitsch, D. & Vilotte, J.-P., 1998. The spectral element method: An efficient tool to simulate the seismic response of 2D and 3D geological structures, *Bull. seism. Soc. Am.,* **88**(2), 368–392.

Komatitsch, D., Vilotte, J.-P., Vai, R., Castillo-Covarrubias, J.M. & Sánchez-Sesma, F.J., 1999. The spectral element method for elastic wave equations—application to 2-D and 3-D seismic problems, *Int. J. Numer. Methods Eng.,* **45**(9), 1139–1164.

Lambert, M.-A., Schmalholz, S.M., Saenger, E.H. & Steiner, B., 2009. Low-frequency microtremor anomalies at an oil and gas field in Voitsdorf, Austria, *Geophys. Prospect.,* **57**(3), 393–411.

Lehujeur, M., Vergne, J., Schmittbuhl, J. & Maggi, A., 2015. Characterization of ambient seismic noise near a deep geothermal reservoir and implications for interferometric methods: a case study in northern Alsace, France, *Geotherm. Energy,* **3**(1), 3, doi: 10.1186/s40517-014-0020-2

Levander, A.R. & Hill, N.R., 1985. P-SV resonances in irregular low-velocity surface layers, *Bull. seism. Soc. Am.,* **75**(3), 847–864.

Mcnamara, D. & Buland, R., 2004. Ambient Noise Levels in the Continental United States, *Bull. seism. Soc. Am.,* **94,** 1517–1527.

Monteiller, V., Chevrot, S., Komatitsch, D. & Fuji, N., 2013. A hybrid method to compute short-period synthetic seismograms of teleseismic body waves in a 3-D regional model, *Geophys. J. Int.,* **192**(1), 230–247.

Mooney, H.M. & Bolt, B.A., 1966. Dispersive characteristics of the first three Rayleigh modes for a single surface layer, *Bull. seism. Soc. Am.,* **56**(1), 43–67.

Nishida, K., 2017. Ambient seismic wave field, *Proc. Japan Acad. B,* **93**(7), 423–448.

Parolai, S. & Richwalski, S.M., 2004. The importance of converted waves in comparing H/V and RSM site response estimates, *Bull. seism. Soc. Am.,* **94**(1), 304–313.

Riahi, N., Goertz, A., Birkelo, B. & Saenger, E.H., 2013. A statistical strategy for ambient seismic wavefield analysis: investigating correlations to a hydrocarbon reservoir, *Geophys. J. Int.,* **192**(1), 148–162.

Saenger, E. *et al.*, 2009. A passive seismic survey over a gas field: analysis of low-frequency anomalies, *Geophysics,* **74**(2), O29–O40.

Seriani, G. & Priolo, E., 1994. Spectral element method for acoustic wave simulation in heterogeneous media, *Finite Elem. Anal. Des.,* **16**(3), 337–348.

Stacey, R., 1988. Improved transparent boundary formulations for the elastic-wave equation, *Bull. seism. Soc. Am.,* **78**(6), 2089–2097.

Steimen, S., 2003. Identifying 2D Resonance in Microtremor Wave Fields, *Bull. seism. Soc. Am.,* **93**(2), 583–599.

Withers, M.M., Aster, R.C., Young, C.J. & Chael, E.P., 1996. High-frequency analysis of seismic background noise as a function of wind speed and shallow depth, *Bull. seism. Soc. Am.,* **86**(5), 1507–1515.

Woodhouse, J.H., 1974. Surface Waves in a Laterally Varying Layered Structure, *Geophys. J. Int.,* **37**(3), 461–490.

APPENDIX A: 3-D MODELLING TECHNIQUES

A1 3-D spectral-element modelling

The method used for the numerical simulations of wave propagation is the Spectral-Element method, SEM (Komatitsch & Vilotte 1998; Komatitsch *et al.* 1999; Chaljub *et al.* 2007). The modelling of 3-D propagation is performed using SPECFEM3D which is an open-source code (Komatitsch *et al.* 1999). The spectral-element is a high order finite element method, FEM, based on the weak formulation of the partial differential equations. Unlike the classic FEM, the mass matrix is diagonal by construction and can be easily inverted. This reduces the computational cost and allows an efficient parallel implementation with distributed memory (Seriani & Priolo 1994; Komatitsch & Vilotte 1998). The method is shown to work accurately with a low number of grid points per Rayleigh minimum wavelength (five points per wavelength compared to 15 in the finite difference method (Komatitsch & Vilotte 1998). The SEM combines spectral methods accuracy and fast convergence with FEM geometrical flexibility (Seriani & Priolo 1994). That is what motivated us to choose the SEM method in our simulations. Parallel implementation is an important aspect to reduce the computational cost. The SEM mesh is restricted to unstructured hexahedral elements in 3-D. In each 3-D hexahedral element of eight nodes, we have $(N + 1)^3$ grid points with $N + 1$ the number of Gauss–Lobatto–Legendre integration points. The sources used in simulations on SPECFEM3D are point forces used with Ricker wavelets as source functions. The position and direction of the source in the 3-D model define the type of waves we get in the interest zone (where the receivers are located). Sources located close enough to the surface generate preferably surface waves. Sources located far from the interest zone allow us to get a well separated surface wave train. In case of a layered model, fundamental mode of surface waves is dominant when the source is close to the surface and higher modes when the source is deeper. The boundary condition we use in SPECFEM3D is the Stacey absorbing condition. The method was initially developed by Clayton & Engquist (1977) and improved by Stacey (1988). It relies on a simple paraxial approximation of the wave equation. A first-order approximation close to that of Stacey (1988) is proposed by Komatitsch & Vilotte (1998) in which the traction at the boundaries is given by:

$$\mathbf{T} = V_P \rho [\mathbf{v}.\mathbf{n}]\mathbf{n} + V_S \rho \mathbf{v}_\mathbf{T}, \tag{A1}$$

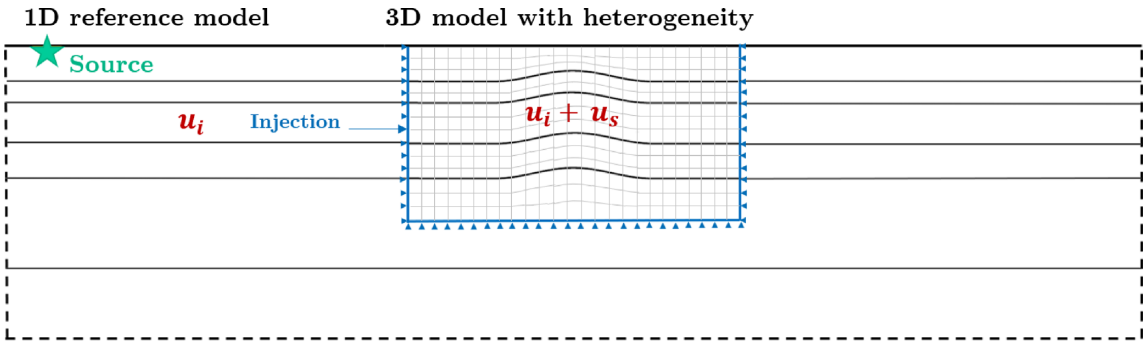

Figure A1. The 3-D model with limited dimensions contains the heterogeneity (central part). The source is excited in a 1-D reference model and the wavefield is injected on the boundaries of the 3-D model. The model properties at the lateral and bottom boundaries (blue lines) of the 3-D model are the same as for the 1-D reference model.

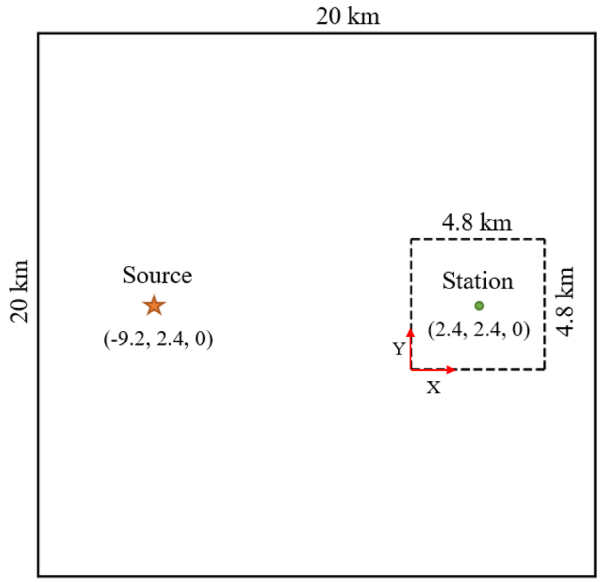

Figure A2. Horizontal projection of the large model used for a standard SPECFEM3D simulation and the small model used with the coupling technique. This figure shows of the source and the receiver positions relative to the X-Y axis.

where $\mathbf{T}$ is the traction vector on the boundary, $\mathbf{n}$ is the unit outward normal to the boundary surface, $\mathbf{v_T} = \mathbf{v} - [\mathbf{v}.\mathbf{n}]\mathbf{n}$ is the tangential component of the velocity on the boundary, V_P and V_S are the P and S wave velocities respectively and ρ the density. This boundary condition is accurate for waves reaching the boundaries at angles close to the normal direction. For high angles, spurious reflections on the edges of the model appear. The only way to prevent spurious reflections from contaminating the interest zone would be by increasing the model dimensions, but for 3-D models this has a high computational cost. Another solution that could be more accurate are the 'Perfectly matched layers' (Berenger 1994), but they are more difficult to implement and they increase the computational cost. We managed to keep working with the Stacey boundary conditions by avoiding as much as possible the influence of the spurious reflections by coupling the spectral-element modelling with analytical modelling at the model boundaries.

A2 Coupling of analytical and spectral-element modelling

The method described here is a combination of analytical solution of wave propagation for surface waves in a 1-D heterogeneous medium (2.1) with SPECFEM3D numerical modelling. As a result of the wave equation, the total wavefield in a heterogeneous medium can be written as the sum of an incident wavefield in a reference medium and a scattered wavefield in the medium with perturbations due to the heterogeneity (Monteiller *et al.* 2013; Beller 2017):

$$\mathbf{u} = \mathbf{u_i} + \mathbf{u_s}. \tag{A2}$$

In our study, the incident wavefield results from the propagation of surface waves in a reference model. This reference model is a 1-D layered model. The full 3-D model contains a heterogeneity which causes the creation of a scattered wavefield (an anticline in our case, Fig. A1). On the boundary between the 1-D reference model and the 3-D heterogeneous model, the incident wavefield is known: it is given by the analytical resolution of the wave propagation equation for surface waves in a laterally homogeneous medium as described in Section 2.1.

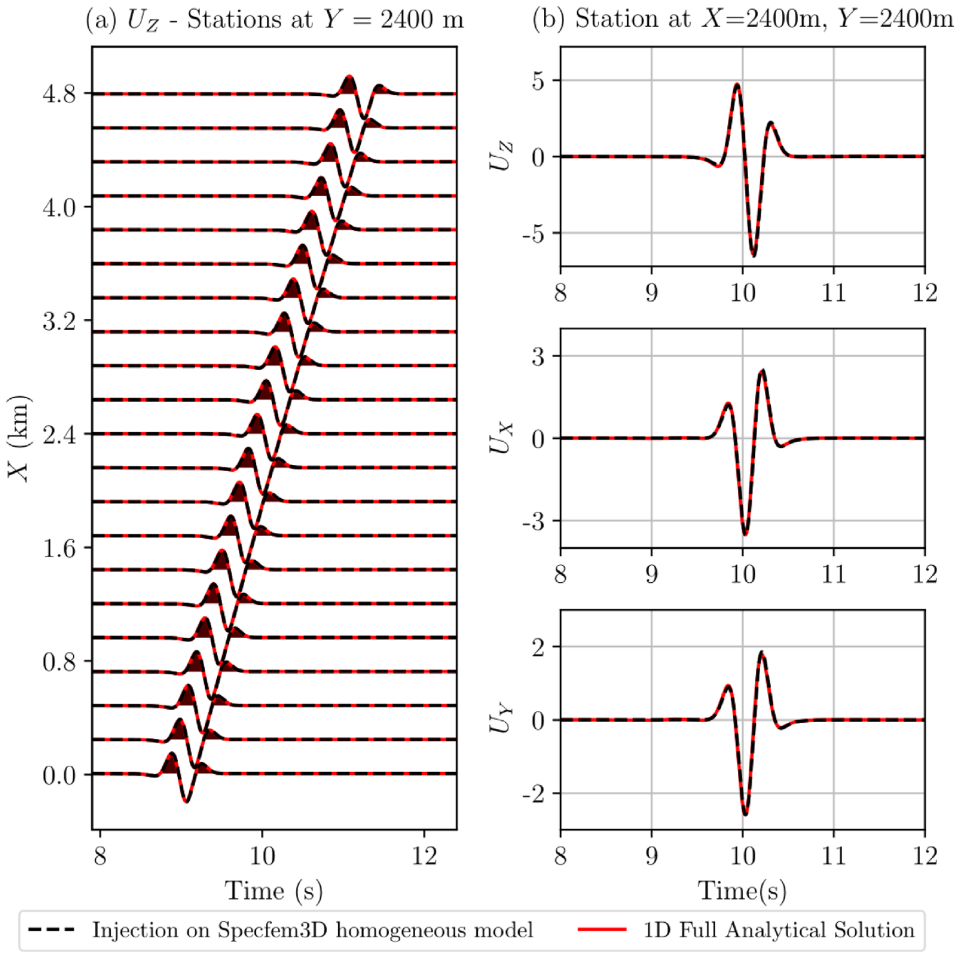

Figure A3. Surface waves injection method validation for Rayleigh waves in a homogeneous model: (a) U_Z for a line of stations at surface, (b) U_Z, U_X and U_Y at one station at surface.

In order to let the far incident wavefield interact with the heterogeneity, we proceed to the injection of this wavefield at the lateral and bottom boundaries of the full 3-D model. The properties of the medium at the injection boundaries must be the same as the properties of the 1-D reference model. The velocity $\mathbf{v_i}$, and traction $\mathbf{T_i}$ resulting from the 1-D analytical solution of wave propagation for surface waves are calculated at each point of the mesh at the lateral and bottom boundaries of the 3-D model, including all the GLL points. The traction vector $\mathbf{T_i}$ is derived from the stress tensor which can be determined as function of the spacial derivatives of the displacement vector. For that, eq. (7.28) in Aki & Richards (2002) is used.

The injection is done by using the Stacey absorbing boundary condition (eq. A1). In this equation implemented in the SPECFEM3D code, we replace the traction and velocity vectors by the scattered tractions and velocities $\mathbf{T_s} = \mathbf{T} - \mathbf{T_i}$ and $\mathbf{v_s} = \mathbf{v} - \mathbf{v_i}$. The equation becomes:

$$\mathbf{T} - \mathbf{T_i} = V_P \rho[(\mathbf{v} - \mathbf{v_i}).\mathbf{n}]\mathbf{n} + V_S \rho(\mathbf{v} - \mathbf{v_i})_T. \tag{A3}$$

In this way, the absorbing boundary equation works to absorb the diffracted wavefield. When the perturbations in the 3-D model are not very pronounced compared to the reference model, the diffracted field is well absorbed by the absorbing condition.

A2.1 Validation

The injection technique was tested for surface waves and validated by superposing two types of seismograms: one obtained with a full 1-D analytical simulation of surface waves, and the other obtained by injecting the solution of the analytical equation at the boundaries of a on small SPECFEM3D model of dimensions 4800 m × 4800 m × 920 m. The source is located outside the 3-D model, at X = −9000 m, Y = −6000 m, Z = 80 m (Fig. A2). Fig. A3 shows a comparison between the two approaches in the case of a homogeneous model for the fundamental Rayleigh wave mode. The seismograms fit perfectly. A complementary validation is illustrated in Fig. A4 but it will be explained in the next paragraph because it is also a confirmation of the advantages of the coupling method.

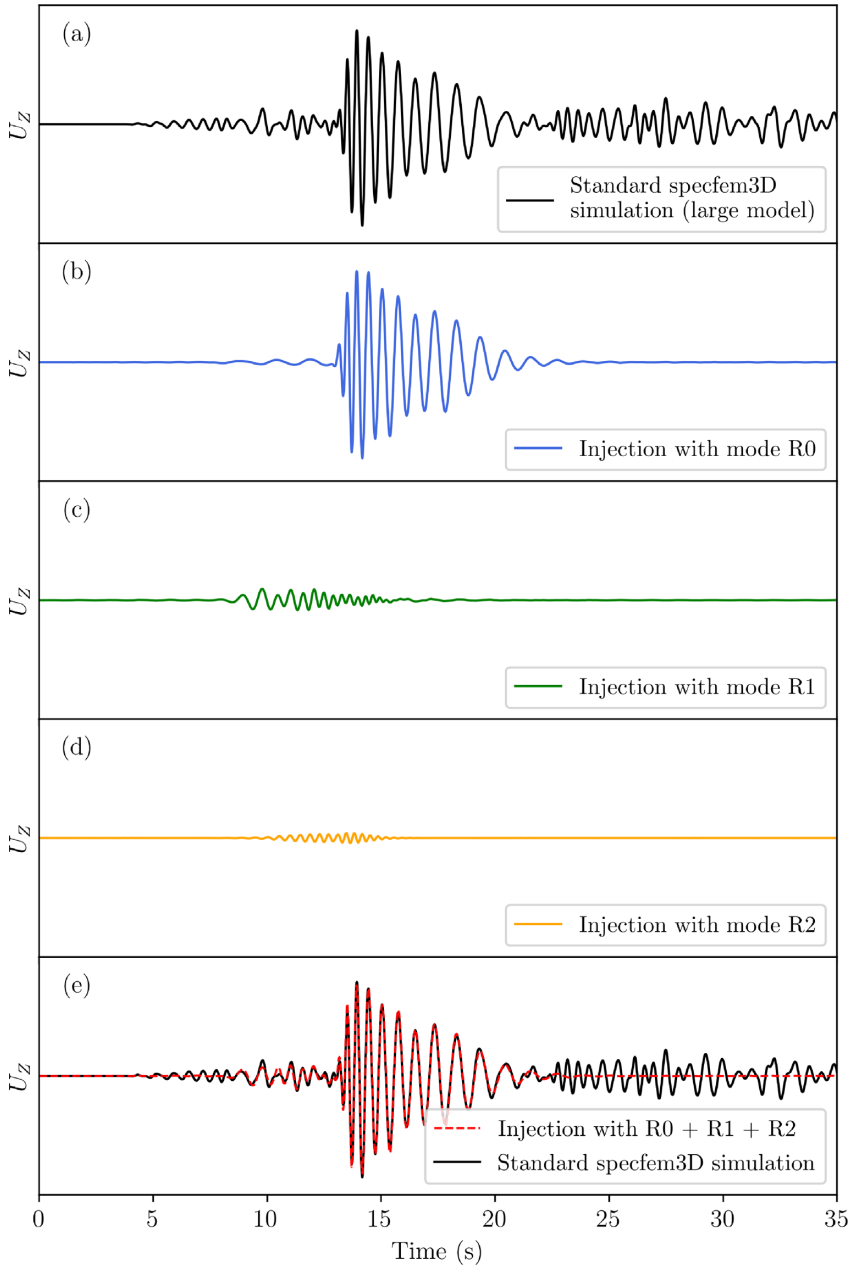

Figure A4. Vertical displacement outputs of (a) a standard SPECFEM3D simulation using a large model, (b,c,d) a simulation with the coupling technique on a small 3-D model using R0, R1 and R2 modes. (e) Superposition of the standard simulation output and the sum of the injection output with R0, R1 and R2 modes.

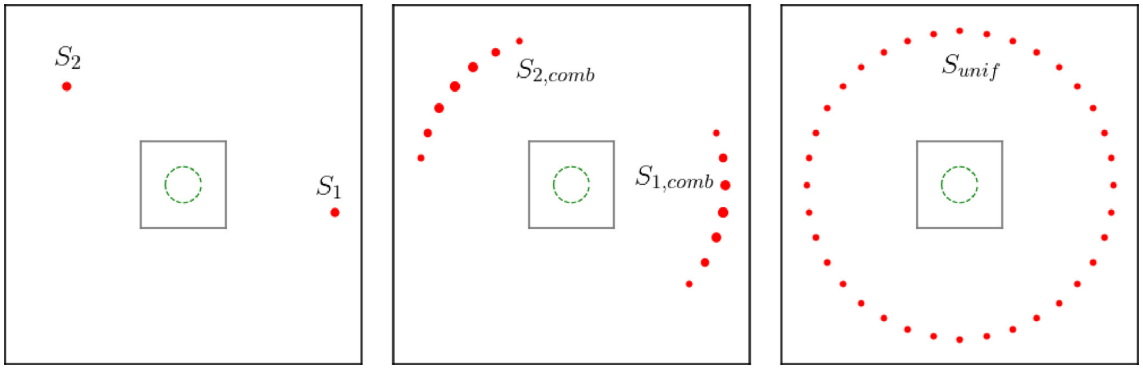

Figure A5. Different source distributions used for studying the anticline effect. From left to right: two single azimuth sources (S_1 and S_2), two source combinations of 30° azimuth range with a normal distribution of weights around the central source ($S_{1,\,\mathrm{comb}}$ and $S_{2,\,\mathrm{comb}}$), (c) uniform distribution of sources along the azimuths (S_{unif}). The grey square represents the 3-D model XY surface plane and the green dotted circle represents the anticline projection.

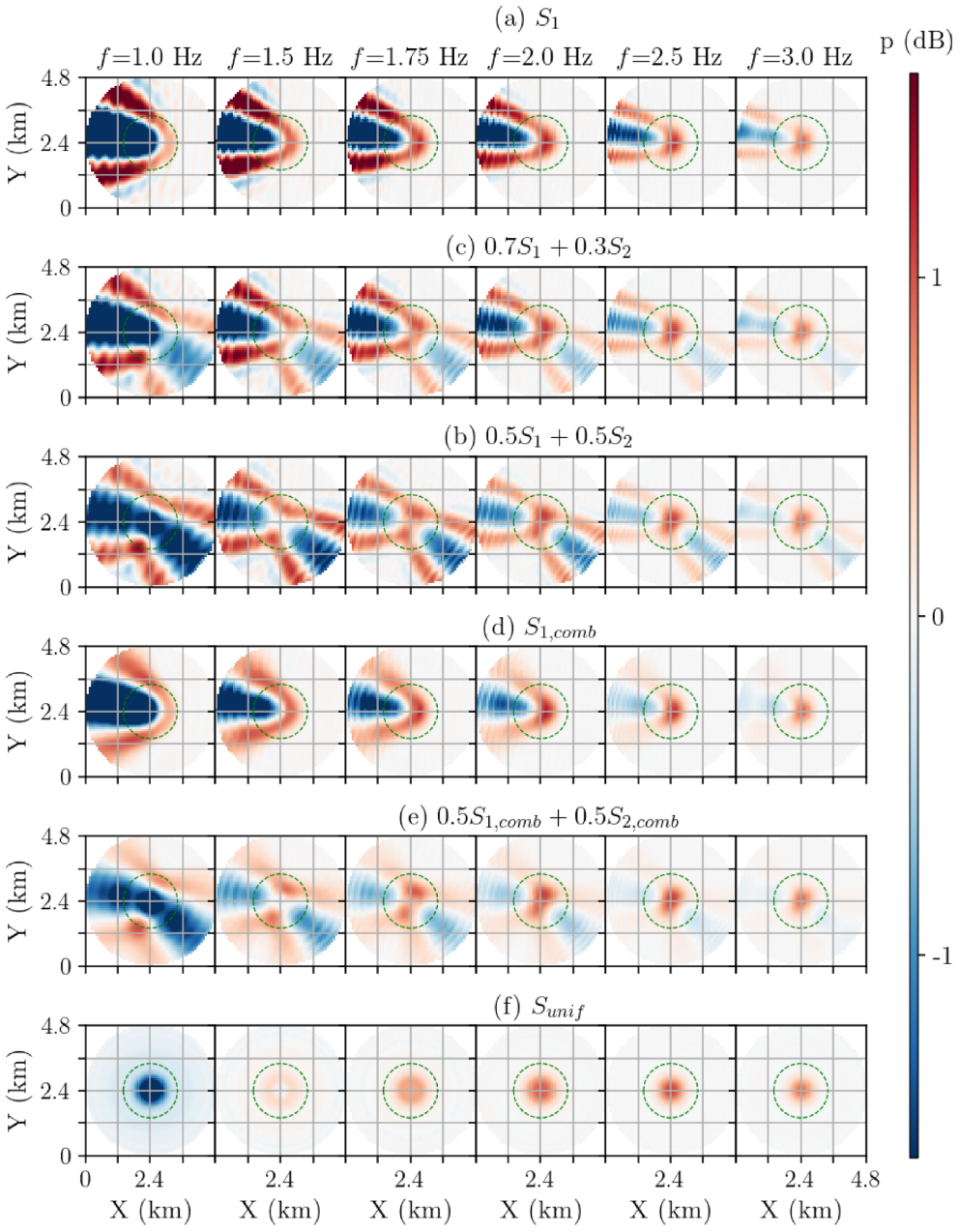

Figure A6. Anticline-induced anomaly (attribute p) maps at the surface for different frequencies, computed for different source combinations illustrated in Fig. A5.

A2.2 Advantages

This method is very efficient because it only requires the knowledge of the incident wavefield at the boundaries of a small 3-D model. The biggest advantage is that it allows us to reduce the 3-D model size, restricting it to a small domain including the heterogeneity, without being influenced by reflections on boundaries. The reduction of model size reached a factor around 4.2 in each horizontal direction and a factor of 2 in the vertical direction. This implies $4.2 \times 4.2 \times 2 \approx 35$ times less computational time. However, we should not forget the time needed to compute the analytical solution on each GLL point of the model boundaries. In addition, using this method we were able to inject specific Rayleigh wave modes, without contamination from body waves or overtones that are detected when doing a standard simulation on SPECFEM3D with point sources embedded in the 3-D model.

As an example, we consider a small 3-D model of dimensions 4.8 km × 4.8 km × 1.04 km and a large 3-D model with the same layer properties and with dimensions 20 km × 20 km × 2 km. The source is located at the surface outside the small model and inside the large model ($X = -9.2$ km, $Y = 2400$ km, $Z = 0$ relative to the small model coordinate axis, Fig. A2). For the sake of comparison, a standard SPECFEM3D is performed on the large model and the vertical displacement output is plotted as a function of time at a receiver located at the surface and at the centre of the small model (Fig. A4a). On the other hand, simulations using the coupling technique are performed with

a single Rayleigh wave mode (modes R0, R1 and R2, Figs A4b,c,d). The coupling technique reduces the total computational time by a factor 12 compared to the standard simulation. In Fig. A4(e), we overlay the standard simulation output to the sum of the injection outputs with R0, R1 and R2 modes. In the standard simulation, parts of the signal are body waves direct arrivals and reflections on the model edges. These unwanted signals are not present with the coupling technique on a small model.

APPENDIX B: 3-D SIMULATIONS WITH DIFFERENT SOURCE COMBINATIONS

In this part, we present the results of anticline-induced anomalies obtained when combining different source distributions (Figs A5, A6). In real data, we usually have sources originating from one or more specific azimuths or ranges of azimuths. With a symmetrical 3-D model with respect to a vertical axis passing by the central station, a rotation of the source results in a rotation of the PSD_Z maps, so we do not need to repeat the 3-D simulation for different source azimuths. Under the assumption of uncorrelated sources from different azimuths, the final PSD_Z can be obtained as a linear average of the different contributions. Thus we are able to rotate the source, combine different sources and add specific weights to each source.